



Published in final edited form as:

Nature. ; 480(7376): 268–272. doi:10.1038/nature10577.

## Atomic resolution dynamics on the surface of amyloid $\beta$ protofibrils probed by solution NMR

Nicolas L. Fawzi<sup>1</sup>, Jinfa Ying<sup>1</sup>, Rodolfo Ghirlando<sup>2</sup>, Dennis A. Torchia<sup>3</sup>, and G. Marius Clore<sup>1</sup>

<sup>1</sup>Laboratories of Chemical Physics, National Institute of Diabetes and Digestive and Kidney Diseases, National Institutes of Health, Bethesda, Maryland 20892-0520, U.S.A.

<sup>2</sup>Molecular Biology, National Institute of Diabetes and Digestive and Kidney Diseases, National Institutes of Health, Bethesda, Maryland 20892-0520, U.S.A.

<sup>3</sup>National Institute of Dental and Craniofacial Research, National Institutes of Health, Bethesda, Maryland 20892-0520, U.S.A.

### Abstract

Exchange dynamics between molecules free in solution and bound to the surface of a large supramolecular structure, a polymer, a membrane or solid support are important in many phenomena in biology and material science. Here we present a novel and generally applicable solution NMR technique, known as Dark-state Exchange Saturation Transfer (DEST), to probe such exchange phenomena with atomic resolution. This is illustrated by the exchange reaction between amyloid  $\beta$  (A $\beta$ ) monomers and polydisperse, NMR invisible ('dark') protofibrils, a process of significant interest since the accumulation of toxic, aggregated forms of A $\beta$ , from small oligomers to very large assemblies, have been implicated in the etiology of Alzheimer's disease<sup>1–6</sup>. The <sup>15</sup>N-DEST experiment imprints with single residue resolution dynamic information on the protofibril-bound species in the form of <sup>15</sup>N transverse relaxation rates (<sup>15</sup>N- $R_2$ ) and exchange kinetics between monomers and protofibrils onto the easily observed two-dimensional <sup>1</sup>H-<sup>15</sup>N correlation spectrum of the monomer. The exchanging species on the protofibril surface comprise an ensemble of sparsely-populated states where each residue is either tethered to (via other residues) or in direct contact with the surface. The first eight residues exist predominantly in a mobile tethered state, while the largely hydrophobic central region and part of the C-terminal hydrophobic region are in direct contact with the protofibril surface for a significant proportion of the time. The C-terminal residues of both A $\beta$ 40 and A $\beta$ 42 display lower affinity for the protofibril surface indicating that they are likely to be surface exposed rather than buried as in structures of A $\beta$  fibrils<sup>7–10</sup>, and may therefore comprise the critical nucleus for fibril formation<sup>11,12</sup>. The <sup>15</sup>N –  $R_2^{tethered}$  values, however, are significantly larger for the C-terminal

Users may view, print, copy, download and text and data- mine the content in such documents, for the purposes of academic research, subject always to the full Conditions of use: [http://www.nature.com/authors/editorial\\_policies/license.html#terms](http://www.nature.com/authors/editorial_policies/license.html#terms)

Correspondence and requests for materials should be addressed to G.M.C. ([mariusc@mail.nih.gov](mailto:mariusc@mail.nih.gov)).

**Supplementary information** is linked to the on-line version of the paper at [www.nature.com/nature](http://www.nature.com/nature).

**Author contributions** All authors contributed extensively to the work described in this paper.

**Author information** The authors declare no competing financial interests. Readers are welcome to comment on the online version of this article at [www.nature.com/nature](http://www.nature.com/nature).

residues of A $\beta$ 42 than A $\beta$ 40 which may explain the former's higher propensity for rapid aggregation and fibril formation<sup>13,14</sup>.

We recently reported the existence of a dynamic exchange process under pseudo-equilibrium conditions between monomeric and very high molecular weight, soluble species of A $\beta$ 40<sup>15</sup>. The latter form spontaneously in concentrated (150–300  $\mu$ M) unstirred aqueous solution, and comprise polydisperse, non-fibrillar aggregates typical of worm-like protofibrils (Fig. S1a). Similar protofibrils are formed by A $\beta$ 42 under the same conditions (Fig. S1b). These protofibrils, which we have characterized extensively by atomic force and electron microscopy (Fig. S1), analytical ultracentrifugation (Fig. S3) and dynamic light scattering (Fig. S4) are far too large (1.8–85 MDa) to detect directly using solution NMR spectroscopy as their resonances are broadened beyond detection<sup>15</sup>, and their heterogeneous nature makes biophysical characterization challenging<sup>5,16–19</sup>. Both the A $\beta$ 40 and A $\beta$ 42 protofibrils present in the equilibrated concentrated samples react strongly with the OC polyclonal antibody that recognizes so-called "fibrillar" oligomers and fibrils<sup>3</sup> (Fig. S6b); the A11 polyclonal antibody recognizes so-called "pre-fibrillar" oligomers<sup>3</sup> and reacts with both A $\beta$ 40 and A $\beta$ 42 protofibrils, albeit weakly with the former (Fig. S6a). The predominantly unstructured, intrinsically disordered, monomeric A $\beta$  peptides<sup>20,21</sup>, however, give rise to excellent solution NMR spectra<sup>15</sup> (Fig. S7), and analytical ultracentrifugation indicates unambiguously that the NMR visible species is monomeric, and that there are no measurable quantities of low molecular weight oligomers present in either the dilute (Fig. S2) or concentrated (Fig. S5) samples. Indeed, in the concentrated samples containing monomer and protofibrils, there is no evidence by analytical ultracentrifugation of any species other than monomer and protofibrils with  $M_r$  in excess of 1.8 MDa (Figs. S4 and S5). In this work, we probe the protofibril-bound species at a residue-by-residue level using <sup>15</sup>N-DEST, a novel two-dimensional transfer-of-saturation NMR experiment that exploits the exchange process between NMR invisible ('dark state') and easily observed monomeric states.

The essence of the 2D <sup>15</sup>N-DEST experiment is based on the dramatic reduction in reorientational motions upon binding to the surface of the protofibrils resulting in transverse relaxation rates (<sup>15</sup>N- $R_2$ ) that are orders of magnitude larger than those of the free monomer. These large <sup>15</sup>N- $R_2$  values preclude direct observation by solution NMR, but allow for efficient partial saturation of <sup>15</sup>N longitudinal magnetization of the protofibril-bound form by a weak radiofrequency (RF) field, even at large offsets where the free monomer magnetization is completely unaffected. In the DEST experiment <sup>15</sup>N longitudinal magnetization of the free monomer is prepared (refocused INEPT transfer), transferred by chemical exchange to the protofibril-bound form (binding), partially saturated (weak <sup>15</sup>N saturation at a series of offsets), and transferred back to the free monomer (dissociation) where the partial saturation is recorded as an attenuation of the cross-peaks of the NMR observable free monomer relative to that in a reference spectrum obtained without saturation (see Full Methods and Fig. S8).

NMR measurements were made at 10°C, pH 6.8 using two concentrations of A $\beta$ : a low concentration sample (50  $\mu$ M) at which both A $\beta$ 40 and A $\beta$ 42 remain nearly entirely

monomeric (>90%) for a long period of time (>2 months for A $\beta$ 40 and ~1 week for A $\beta$ 42) based on cross-peak intensities in a  $^1\text{H}$ - $^{15}\text{N}$  heteronuclear single quantum coherence correlation (HSQC) spectrum; and a higher concentration sample in which the fraction of monomer decreases rapidly (over ~2 days for A $\beta$ 42 and ~1 week for A $\beta$ 40) after which a stable pseudo-equilibrium between monomer and protofibrils is maintained for more than a week<sup>15</sup> (Fig. S9). The amount of protofibrils formed at a given initial concentration of A $\beta$  is significantly higher for A $\beta$ 42 than A $\beta$ 40 (Fig. S9). Thus, for 270  $\mu\text{M}$  A $\beta$ 40 and 160  $\mu\text{M}$  A $\beta$ 42 samples, the concentration of monomer decreases to pseudo steady-state levels of ~110 and ~35  $\mu\text{M}$ , respectively.

For the monomeric A $\beta$ 40 sample, the  $^1\text{H}$ - $^{15}\text{N}$  cross-peaks in the DEST experiment display an extremely sharp saturation profile with no detectable attenuation for any residue until the saturation pulse is less than 2 kHz from the  $^{15}\text{N}$  resonance frequencies of the monomer (Fig. 1a, circles). This behavior, replicated for the monomeric A $\beta$ 42 sample, matches the predicted saturation profile for a  $^{15}\text{N}$  spin with relaxation parameters measured for the monomeric species (Fig. 1a, solid line). In contrast, the  $^1\text{H}$ - $^{15}\text{N}$  cross-peaks in the 270  $\mu\text{M}$  A $\beta$ 40 sample show significant partial saturation at offsets far from the monomer  $^{15}\text{N}$  resonances. Most importantly, the saturation profiles are clearly residue specific (Fig. 1b–d, circles). Relatively narrow profiles are observed for residues in the N-terminal region (Fig. 1b), very broad profiles for residues in the central (residues 17 to 21, e.g. Fig. 1c) and part of the C-terminal (residues 30 to 40) hydrophobic regions. Intermediate profiles are observed for residues in the hydrophilic region spanning residues 25 through 29 (Fig. 1d) as well as for the three C-terminal residues. Qualitatively similar behavior is observed for the 160  $\mu\text{M}$  A $\beta$ 42 sample (Fig. S10a–d). The observed residue-specific saturation transfer profiles indicate that, when bound to the surface of the protofibrils, the average  $^{15}\text{N}$ - $R_2$  for each residue is highly sequence-position dependent.

The  $^{15}\text{N}$ -DEST profiles can be quantitatively interpreted by incorporating a model of equilibrium chemical exchange within the framework of the McConnell equations<sup>22,23</sup>. The simplest model describing the equilibrium between free monomer ( $M_{\text{monomer}}$ ) and peptide transiently bound to the surface of the protofibril ( $M_{\text{oligomer}}$ ) is a pseudo-first-order process characterized by global first order apparent association ( $k_{\text{on}}^{\text{app}}$ ) and dissociation ( $k_{\text{off}}$ ) rate constants (Fig. 2a) and residue-specific  $^{15}\text{N}$ - $R_1$  (longitudinal) and  $R_2$  (transverse) values for the free monomer and protofibril-bound states. The value of the  $k_{\text{on}}^{\text{app}}$  can be estimated from the difference,  $R_2$ , in  $^{15}\text{N}$ - $R_2$  values between the samples with protofibrils present and the monomeric reference sample (50  $\mu\text{M}$ )<sup>15</sup>. Since transverse magnetization for the protofibril-bound states decay extremely rapidly, the maximum observed  $R_2$  value,  $\Delta R_2^{\text{max}}$ , is equal to  $k_{\text{on}}^{\text{app}}$  under pseudo-equilibrium conditions (note that the observed  $R_2$  values are independent of nucleus and magnetic field<sup>15</sup>; see also Supplementary section 5 for a simple explanation of  $R_2$  and DEST experiments and their interpretation). The saturation profiles at two RF field strengths (170 and 350 Hz) and the  $R_2$  data for all residues (Fig. 1e for A $\beta$ 40 and Fig. S10e for A $\beta$ 42) were fit simultaneously optimizing the values of  $k_{\text{on}}^{\text{app}}$  and  $k_{\text{off}}$ , and the residue specific  $^{15}\text{N}$ - $R_2$  values for the protofibril-bound species (see full Methods). The  $^{15}\text{N}$ - $R_1$  and  $R_2$  values for the monomer were taken from relaxation data recorded on the low concentration (50  $\mu\text{M}$ ) sample. Although the  $^{15}\text{N}$ - $R_1$  values for the protofibril-bound

state are unknown, these  $^{15}\text{N}-R_1$  values have no effect on the fitted parameters within their uncertainties over the expected range ( $2 \text{ s}^{-1} < ^{15}\text{N}-R_1 < 0.01 \text{ s}^{-1}$ ) due to the design of the experiment (see full Methods). The simple two-state model fails to account simultaneously for all the experimental data in the case of both A $\beta$ 40 (Fig 1b–e) and A $\beta$ 42 (Fig. S10), with systematic deviations for the DEST profiles (Figs. 1b–d, dashed lines) and failure to reproduce  $R_2$  as a function of sequence (Fig. 1e, grey open circles). Extension to a three-site exchange model that adds an intermediate species *either* on- or off-pathway, introducing additional unknown rate constants connecting monomer, intermediate and protofibril-bound states and residue-specific  $^{15}\text{N}-R_2$  values for the intermediate state, also fails to fit the experimental data.

The above results led us to investigate a simple modification of the two-state model in which the ensemble of protofibril-bound states is divided into two subsets where a given residue is either in direct contact with the protofibril surface ( $I_{\text{contact}}$ ) or tethered ( $I_{\text{tethered}}$ ) via residues in direct contact with the protofibril (Fig. 2b). The key to understanding this model lies in the observation that the variations in *both*  $R_2$  and  $^{15}\text{N}$ -DEST profiles are residue specific. This variation cannot be accounted for by postulating the existence of low molecular weight oligomers since, in that case, the  $R_2$  and DEST effects would be uniform throughout the peptide sequence (as each residue would be subject to the same events and the same average relaxation behavior when bound to the surface of the oligomers). Thus for each residue,  $i$ , there is a potentially different partitioning of the large number of conformational states into  $I_{\text{tethered}}(i)$  and  $I_{\text{contact}}(i)$ . This partitioning is computed for a single residue at a time, the state of the other residues may be tethered, bound or interconverting between the two, and the correlation between states at different positions is not considered. Critical to the simplicity of the model is the retention of the overall two-state association/dissociation process; the global apparent association rate constant for the conversion of monomer to the protofibril-bound ensemble,  $k_{\text{on}}^{\text{app}}$ , is given by the sum of the pseudo-first order rate constants  $k_1^{\text{app}}(i)$  and  $k_2^{\text{app}}(i)$  for the conversion of a residue  $i$  from the monomeric state ( $I_{\text{monomer}}$ ) to  $I_{\text{tethered}}(i)$  and  $I_{\text{contact}}(i)$ , respectively; the global dissociation rate constant,  $k_{\text{off}}$ , from protofibril-bound states to monomer is the same for  $I_{\text{tethered}}(i)$  and  $I_{\text{contact}}(i)$  for all residues  $i$  (i.e.  $k_{\text{off}} = k_{-1} = k_{-2}$ ). Thus, the two-state equilibrium between monomer and protofibril-bound forms is preserved, and  $k_{\text{on}}^{\text{app}}$  and  $k_{\text{off}}$  represent ensemble averaged rates. This model adds the fewest parameters to describe a system with a huge number of potential configurations ( $2^{40}$  and  $2^{42}$  for A $\beta$ 40 and A $\beta$ 42, respectively, where each residue is represented as either tethered or in direct contact) with differing behavior at each residue. Since there are so many combinations of states, the addition of further variation from the polydispersity of the protofibrils does not impact the interpretation of the data or its quantitative analysis in terms of the model in Fig. 2b.

A residue-specific equilibrium between the tethered and direct-contact states is described by the ratio of  $I_{\text{contact}}(i)$  to  $I_{\text{tethered}}(i)$ ,  $K_3(i) = k_2^{\text{app}}(i)/k_1^{\text{app}}(i)$ . Direct interconversion between  $I_{\text{contact}}(i)$  and  $I_{\text{tethered}}(i)$  is not necessary to fit the data and, hence, is not incorporated in the analysis presented in the main text (see Table S1 and Figure S11 for analysis including these kinetic paths). The  $^{15}\text{N} - R_2^{\text{tethered}}$  values for the  $I_{\text{tethered}}$  states are also residue-specific and describe the average dynamics of a given residue in the tethered state. In physical terms, this

will depend upon the average length and flexibility of the segment separating residue  $i$  from other residues of the peptide in direct contact with the oligomer.

The model in Fig. 2b is a reduced, “model-free” representation of the actual system which clearly comprises a large ensemble of different states and interconversion networks. Although the model is phenomenological in that individual protofibril-bound states in the ensemble and the correlated behavior of residues are not explicitly considered, the smooth variation of the fitted parameters as a function of residue is indicative of correlated behavior at adjacent positions, as to be expected for a model that well describes physical behavior. Further, the model does not require that a single protofibril state be present or that the members of the protofibril ensemble even have the same interfaces with bound monomers. The ability to interpret the experimentally observed residue-by-residue differences between A $\beta$ 40 and A $\beta$ 42 demonstrates the success of the model.

Least-squares non-linear optimization of the scheme shown in Fig. 2b results in excellent fits to both the  $^{15}\text{N}$ -DEST saturation profiles (Fig. 1b–d and Fig. S10a–d) and the  $R_2$  data (Fig. 1e and Fig. S10e). For A $\beta$ 40 at 270 $\mu\text{M}$ ,  $k_{on}^{app} = 3.0 \pm 0.7 \text{ s}^{-1}$ , in agreement with the observed value of  $3.0 \text{ s}^{-1}$  for  $\Delta R_2^{\text{max}}$  (Fig. 1e), and  $k_{off} = 51 \pm 12 \text{ s}^{-1}$ , in good agreement with our previous estimate of  $\sim 73 \text{ s}^{-1}$  obtained from a one-dimensional  $^1\text{H}$  saturation experiment<sup>15</sup>. The values of  $k_{on}^{app}$  and  $k_{off}$  for A $\beta$ 42 at 160  $\mu\text{M}$  are  $2.4 \text{ s}^{-1}$  (in agreement with  $2.3 \text{ s}^{-1}$  for  $\Delta R_2^{\text{max}}$ ) and  $62 \text{ s}^{-1}$ , respectively, although the standard deviations in these fitted parameters are higher due to lower experimental signal-to-noise ( $\pm 1.8 \text{ s}^{-1}$  and  $\pm 46 \text{ s}^{-1}$ ). The values of  $^{15}\text{N} - R_2^{\text{contact}}$  are  $18,800 \pm 700 \text{ s}^{-1}$  and  $19,300 \pm 2000 \text{ s}^{-1}$  for A $\beta$ 40 and A $\beta$ 42, respectively, which are reasonable for the large, worm-like protofibrils seen in these samples by atomic force and electron microscopy (Fig. S1). From these rate constants one can deduce that the populations of transiently-bound A $\beta$ 40 and A $\beta$ 42 are  $\sim 6\%$  and  $\sim 4\%$ , respectively, that of free monomer.

The residue-specific partitioning,  $K_3(i)$ , between the direct-contact and tethered states (Fig. 3a) and the associated  $^{15}\text{N} - R_2^{\text{tethered}}$  relaxation values (Fig. 3b) provide the first characterization of the protofibril-bound forms of A $\beta$ 40 and A $\beta$ 42 at the single residue level. Qualitatively the  $K_3$  and  $^{15}\text{N} - R_2^{\text{tethered}}$  profiles for A $\beta$ 40 and A $\beta$ 42 are similar, with the notable exception of the  $^{15}\text{N} - R_2^{\text{tethered}}$  values for the C-terminal residues. We also note that the values of  $K_3$  and  $^{15}\text{N} - R_2^{\text{tethered}}$  are directly correlated with the observed widths of the saturation profiles and  $R_2$ , respectively (Fig. S12), demonstrating that the model is consistent with a qualitative analysis of the data suggested directly from the observed residue-specific behavior.

For both A $\beta$ 40 and A $\beta$ 42 the first eight N-terminal residues have similar, small values of  $K_3$  (0.08 to 0.14), indicating that these residues are predominantly tethered, spending only a small fraction ( $\sim 10\%$ ) of the time in actual direct contact with the protofibril surface. Correlated with this finding, these residues retain considerable flexibility as reflected by  $^{15}\text{N} - R_2^{\text{tethered}}$  values ranging from 20 to  $80 \text{ s}^{-1}$ . These observations are consistent with  $^{13}\text{C}$  linewidths in solid state NMR spectra of A $\beta$ 40 fibrils that are indicative of conformational

disorder for the N-terminal segment<sup>10</sup>, although our data indicate a small but measurable population in direct contact with the protofibril surface.

The highest values of  $K_3$  ( $>0.24$ ) are seen for residues 16–25 and 28–37 of A $\beta$ 40 and residues 16–23 and 33–40 of A $\beta$ 42, corresponding roughly to the central and C-terminal hydrophobic regions that form intermolecular  $\beta$ -sheets at the core of amyloid fibrils<sup>9,10</sup>. Although the ratio of direct-contact to tethered states in the A $\beta$ 40 protofibril-bound ensemble is very similar for the two regions ( $0.34\pm 0.06$  versus  $0.32\pm 0.04$ ), the average  $^{15}\text{N} - R_2^{\text{tethered}}$  values are very different:  $146\pm 33 \text{ s}^{-1}$  for residues 16–22 falling to  $61\pm 16 \text{ s}^{-1}$  for residues 23–25, and  $62\pm 13 \text{ s}^{-1}$  for residues 28–37. This suggests that, in the tethered states, residues 28–37 of A $\beta$ 40 are considerably more flexible than residues 16–22. In terms of a physical picture this suggests that the C-terminal region of A $\beta$ 40 may be far from the protofibril surface when other residues (such as the 16–22 region) are bound, while the converse is true for the 16–22 region. For A $\beta$ 42, the average value of  $K_3$  is slightly higher in the central hydrophobic region ( $0.35\pm 0.06$ ) compared to the 33–40 region ( $0.28\pm 0.03$ ), but in contrast to A $\beta$ 40, the corresponding  $^{15}\text{N} - R_2^{\text{tethered}}$  average values are quite similar ( $133\pm 33 \text{ s}^{-1}$  and  $99\pm 35 \text{ s}^{-1}$ , respectively), suggesting that the tethered states of the C-terminal hydrophobic region are on average less mobile and closer to the protofibril surface in A $\beta$ 42 than in A $\beta$ 40.

The most striking differences between protofibril-bound A $\beta$ 40 and A $\beta$ 42 are seen at the C-terminus. Intermediate  $K_3$  values (0.21 to 0.23) associated with low  $^{15}\text{N} - R_2^{\text{tethered}}$  values ( $58, 24$  and  $23 \text{ s}^{-1}$  for residues 38, 39 and 40, respectively) are observed for the last three C-terminal residues of A $\beta$ 40 (Fig. 3). Thus, residues 38–40 in the ensemble of A $\beta$ 40 protofibril-bound states are more mobile and hence significantly less often buried than the central (residues 16–25) and C-terminal (residues 28–37) hydrophobic regions. This is in sharp contrast to A $\beta$ 40 fibrils where the C-terminal residues are located at the central core of the fiber, forming tight intermolecular contacts with both neighboring strands in the C-terminal cross- $\beta$  sheet and adjacent subunits in the supramolecular structure<sup>9</sup>. Interestingly, the last two C-terminal residues of antibody-stabilized A $\beta$ 40 protofibrils also exhibit increased mobility as assessed by solid state NMR<sup>19</sup>, suggesting that enhanced dynamics of the C-terminal residues of A $\beta$ 40 are at least partially conserved when the protofibril-bound states are incorporated into the protofibril core. Although the population of direct-contact states for the C-terminal residues of A $\beta$ 42 is similar to that of A $\beta$ 40 (Fig. 3a), the corresponding  $^{15}\text{N} - R_2^{\text{tethered}}$  values are significantly higher for A $\beta$ 42 ( $76\pm 16 \text{ s}^{-1}$  for residues 39–42 of A $\beta$ 42 versus  $23.5\pm 0.5 \text{ s}^{-1}$  for residues 39–40 of A $\beta$ 40; Fig. 3b). Thus, the mobility of the C-terminal residues in the tethered states of A $\beta$ 42 are hindered relative to that in A $\beta$ 40.

If dynamics of the C-terminal hydrophobic region and C-terminal residues in the protofibril-bound states, where A $\beta$ 40 and A $\beta$ 42 differ (Fig. 3), constitute the apparent free-energy barrier in the nucleation-dependent conformational change or polymerization separating disordered oligomers from fast-elongating amyloid fibrils<sup>24</sup>, these observed differences may explain the higher rate of protofibril and fibril formation of A $\beta$ 42 relative to A $\beta$ 40<sup>13,14</sup>.

Further, while the population of direct-contact states for the hydrophilic region between residues 27–29 is reduced for both A $\beta$ 40 and A $\beta$ 42, the  $K_3$  values are higher for A $\beta$ 40 than A $\beta$ 42 (Fig. 3a). Since this region constitutes a hairpin turn in A $\beta$  fibrils, the lower population of direct contact states for A $\beta$ 42 may facilitate hairpin and subsequent  $\beta$ -sheet formation, thereby enhancing the rate of incorporation of surface-bound monomers into the protofibril core.

In summary,  $^{15}\text{N}$ -DEST and  $R_2$  measurements probe exchange processes between monomer and protofibril-bound states of A $\beta$  on times scale of 10–100 ms, and imprint the residue-by-residue footprint of the 'dark' protofibril-bound state on the easily observed monomer. These experiments are complementary to pulsed H/D exchange experiments that have been used to probe fibril formation and recycling on a million-fold slower time scale<sup>25,26</sup>, as well as to spin-state selective methyl group relaxation dispersion experiments<sup>27</sup> that probe invisible state dynamics of supramolecular complexes on the intermediate chemical shift time scale of 50  $\mu\text{s}$  to 10 ms<sup>28</sup>. In contrast to relaxation dispersion which requires that the visible and invisible states have different chemical shifts, the DEST and  $R_2$  experiments rely entirely on large differences in transverse relaxation rates ( $R_2$ ). For systems where a relatively small particle (i.e. a macromolecule whose resonances are directly observable by solution NMR) is in exchange with a state bound to a large particle (e.g. an aggregate, a fibril, a large supramolecular complex or a solid support), large differences in  $R_2$  values will be present and consequently the  $R_2$  values in the 'dark' state can be determined by DEST. The DEST experiment requires only that the exchange rate ( $k_{on}^{app} + k_{off}$ ) be larger than the  $^{15}\text{N}$ - $R_1$  of the observed species. The A $\beta$  monomer has a  $^{15}\text{N}$ - $R_1$  of  $\sim 1.5 \text{ s}^{-1}$ , significantly faster and hence more limiting than for a larger protein. Since  $k_{on}^{app}$  is a pseudo-first order rate constant, the use of higher concentrations can increase the apparent on-rate, thereby extending the range of applicability. The upper limit on the value of  $k_{on}^{app}$  is  $\sim 100 \text{ s}^{-1}$ , beyond which accurate determination of  $R_2$  is difficult. We anticipate that the DEST technique for examining dynamics at single residue resolution of otherwise invisible 'dark' states will be applicable to many areas of current interest both in biology (e.g. the interaction of unfolded proteins with the proteasome<sup>29</sup> and very large chaperones, the formation of low-affinity, large supramolecular complexes, the folding-upon-binding<sup>30</sup> of intrinsically disordered proteins) and material science (e.g. exchange reactions on surfaces).

## METHODS SUMMARY

Solutions of uniformly  $^{15}\text{N}$ -labeled A $\beta$ 40 and A $\beta$ 42 were prepared from NaOH-treated stocks as described previously<sup>15</sup>. NMR samples, comprising 50 and 270  $\mu\text{M}$  A $\beta$ 40 and 50 and 160  $\mu\text{M}$  A $\beta$ 42 in 50 mM HEPES, pH 6.8, and 90%  $\text{H}_2\text{O}/10\% \text{D}_2\text{O}$ , were prepared and maintained at 4 to 10  $^\circ\text{C}$  at all times. All NMR experiments were conducted at 10  $^\circ\text{C}$  on a Bruker 900 MHz spectrometer equipped with a triple resonance z-gradient cryoprobe. Fitting the DEST and  $R_2$  data to various kinetic schemes using the McConnell equations to determine the oligomer-bound  $R_2$  values and kinetic parameters was carried out as described in the Full Methods.

**Full Methods** and any associated references are available in the online version of the paper at [www.nature.com/nature](http://www.nature.com/nature).

## METHODS

### Description of the 2D $^{15}\text{N}$ -DEST experiment and pulse sequence

Due to relatively small equilibrium magnetization of  $^{15}\text{N}$  nuclei, initial amide hydrogen ( $^1\text{H}_\text{N}$ ) magnetization for the monomeric species is transferred to longitudinal  $^{15}\text{N}$  magnetization, after which a weak  $^{15}\text{N}$  saturation pulse is applied at a series of radio frequency (RF) offsets (ranging from +35 to -35 kHz) for a sufficient length of time (0.9 s) to allow the monomeric peptide to sample a protofibril-bound state where  $^{15}\text{N}$ - $R_2$  values are orders of magnitude larger than in the monomeric species and allow for efficient partial saturation by the weak RF field. Partial saturation is then transferred back to the monomeric state by chemical exchange, and recorded as a decrease in intensity of the  $^1\text{H}$ - $^{15}\text{N}$  correlation cross-peaks for the NMR observable monomeric species relative to that in a reference spectrum obtained without saturation (see Methods and Fig. S8). Because initial  $^1\text{H}_\text{N}$  to  $^{15}\text{N}$  magnetization INEPT transfer in the high molecular weight protofibrils is extremely inefficient owing to very fast  $^1\text{H}$  and  $^{15}\text{N}$  transverse relaxation, the observed transfer-of-saturation only arises from peptides that begin the experiment as monomers, are incorporated into protofibrils, and subsequently released within the saturation time. The pulse sequence for the 2D HSQC-based  $^{15}\text{N}$ -DEST experiment is shown in Fig. S8. The pulse sequence is similar in spirit to that commonly used for measuring  $^{15}\text{N}$ - $R_1$  longitudinal relaxation except that the variable  $T_1$  relaxation delay is replaced by a weak, continuous wave (CW) saturation pulse at variable radiofrequency (RF) offsets. The DEST experiment begins from the amide proton magnetization  $H_z$  of the monomeric peptide. Following the first INEPT transfer, longitudinal two spin order  $2H_zN_z$  is obtained (Fig. S8, point *a*). The subsequent refocusing INEPT provides in phase  $N_z$  magnetization (Fig. S8, point *b*). The  $90^\circ$   $^1\text{H}$  pulse  $\phi_2$  not only flips the water signal back to the  $+z$  axis, but also purges any residual anti-phase magnetization  $2N_yH_z$  prior to the  $^{15}\text{N}$  CW saturation pulse. The latter is applied for 0.9 s at a series of 15 different offsets (35, 28, 21, 14, 8, 4, 2, 0, -2, -4, -8, -14, -21, -28 and -35 kHz) from the  $^{15}\text{N}$  carrier frequency (set to 118.5 and 117.6 ppm and located at the center of the monomer spectrum of A $\beta$ 40 and A $\beta$ 42, respectively) and at two RF field strengths (170 and 350 Hz). In addition, two reference spectra were recorded at each concentration without saturation. During the CW  $^{15}\text{N}$  pulse, the magnetization ( $N_z$ ) originating from the monomeric peptide is partially saturated when the peptide samples a protofibril-bound state. The latter cannot be directly observed due to extremely rapid transverse ( $R_2$ ) relaxation. This partial saturation results in a reduction of the  $N_z$  magnetization by a multiplicative factor  $\kappa$  (relative to that in the reference spectrum with the saturation pulse turned off) which depends on the strength and frequency of the  $^{15}\text{N}$  saturation pulse as well as on the kinetics of the monomer-oligomer exchange process (see main text for more details), thereby providing valuable insight into the interconversion dynamics at atomic resolution. When the oligomer-bound peptide is released back into solution as a monomer, its reduced magnetization  $\kappa N_z$  is detected via heteronuclear single quantum correlation. It is important to note that inversion of the phases of both the  $90^\circ$   $^1\text{H}$  pulse  $\phi_1$  and the receiver phase alternates the orientation of the  $N_z$  magnetization between



the  $+z$  and  $-z$  axes. Summation of transients with these alternating phases removes non-exponential contributions to longitudinal relaxation (e.g. due to non-zero magnetization at Boltzman equilibrium) so that loss of magnetization due to  $R_1$  relaxation at the end of the CW saturation pulse is a simple scaling factor  $e^{-R_1 t}$ , and hence the  $R_1$  dependence is effectively removed when cross-peak intensities are normalized to those in the spectrum without saturation<sup>31</sup>. Longitudinal cross-correlated relaxation interference between the  $^{15}\text{N}$ - $^1\text{H}$  dipolar interaction and the  $^{15}\text{N}$  chemical shift anisotropy is eliminated by application of the  $180^\circ$   $^1\text{H}$  pulse train (with an interpulse delay of 100 ms) during the CW  $^{15}\text{N}$  pulse. With a cryogenic probe at a  $^1\text{H}$  spectrometer frequency of 900 MHz, this interpulse delay is sufficient to return the water signal back to the  $+z$  axis through radiation damping. The dephasing INEPT following the saturation period results in an anti-phase term  $\kappa 2\text{N}_x\text{H}_z$  (Fig. S8, point *c*). The antiphase  $^{15}\text{N}$  magnetization is then converted to amide proton anti-phase magnetization. The last refocusing INEPT, incorporating a WATERGATE scheme, not only rephases the anti-phase proton magnetization to in-phase  $\kappa\text{H}_x$ , but also suppresses the residual water signal prior to direct detection of the monomeric peptide amide proton magnetization.

### Data Acquisition and Analysis

All NMR experiments were recorded at  $10^\circ\text{C}$  using a Bruker Avance-III spectrometer operating at  $^1\text{H}$  frequency 900.27 MHz and equipped with a Bruker TCI  $z$ -axis gradient cryogenic probe.  $^{15}\text{N}$ - $R_2$  data on the 50 and 270  $\mu\text{M}$  A $\beta$ 40 samples and 50 and 160  $\mu\text{M}$  A $\beta$ 42 samples (prepared as described previously<sup>10</sup>) and  $^{15}\text{N}$ - $R_1$  data at 50  $\mu\text{M}$  were measured using standard interleaved 2D  $^1\text{H}$ - $^{15}\text{N}$  HSQC-based NMR experiments and analyzed as described previously<sup>15</sup>.

The 2D  $^{15}\text{N}$ -DEST spectra were acquired as 32 interleaved experiments (with the RF field strengths and frequencies for the CW  $^{15}\text{N}$  pulse given above). For A $\beta$ 40 each 2D experiment comprises  $154^* \times 1900^*$  complex data points in the indirect  $^{15}\text{N}$  and direct  $^1\text{H}$  dimensions, respectively, with corresponding acquisition time of 77 and 175.6 ms. For A $\beta$ 42  $78^* \times 1900^*$  complex points were acquired with acquisition times of 41 and 175.6 ms. 16 transients for A $\beta$ 40 and 32 for A $\beta$ 42 were collected per FID with a 1.7 s delay between scans. The total experimental times for A $\beta$ 40 and A $\beta$ 42 were each approximately 5 days.

The complete interleaved 2D data set was first split into 32 individual 2D data sets, one for each experiment at a particular  $^{15}\text{N}$  saturation pulse power level and frequency, using a C program written in house. Each experiment was then processed identically and analyzed using NMRPipe<sup>32</sup>. The time-domain data in each spectrum were apodized in the indirect  $^{15}\text{N}$  dimension with a  $54^\circ$ -shifted sine bell function. For the direct  $^1\text{H}$  dimension, an exponential window function with a line broadening of 5 Hz for A $\beta$ 40 and 8 Hz for A $\beta$ 42 was applied, followed in the case of the A $\beta$ 40 data by a  $72^\circ$ -shifted squared sine bell. The additional line-broadening for the A $\beta$ 42 data was used to improve the signal-to-noise owing to the very low ( $\sim 35$   $\mu\text{M}$ ) concentration of free A $\beta$ 42 monomer. Time-domain data in the  $^{15}\text{N}$  and  $^1\text{H}$  dimensions were then zero-filled to obtain a final complex  $1024^* \times 4096^*$  data matrix, with digital resolutions of 2.0 and 2.6 Hz, respectively. The residue-specific signal reduction factor  $\kappa$  as a function of frequency offset of the CW  $^{15}\text{N}$  saturation pulse

was obtained from the ratio of peak heights in the saturation experiment versus the reference experiment with the saturation pulse turned off. (The Bruker pulse sequence and acquisition parameter files for the  $^{15}\text{N}$ -DEST experiment, as well as the processing scripts are available on request.)

### Simultaneous fitting of the DEST and $R_2$ data to kinetic models

A homogenous form of the McConnell equations<sup>22</sup> describing a single spin in chemical exchange, as presented in Eq. 21 of Helgstrand et al.<sup>23</sup>, was expanded to a three-state system. Due to the small gyromagnetic ratio of  $^{15}\text{N}$  nuclei and their sparse density in proteins, cross-relaxation between neighboring  $^{15}\text{N}$  nuclei in both monomer and protofibril-bound states is negligible, in marked contrast with the 1D  $^1\text{H}$  transfer-of-saturation profiles reported previously<sup>15</sup>. Effects on the saturation due to cross-relaxation between  $^{15}\text{N}$  and directly-bonded  $^1\text{H}$  nuclei, though predicted to be small, are removed with phase-cycling, placing the initial  $^{15}\text{N}$  magnetization during the saturation period on the  $+z$  and  $-z$  axes in alternating transients and measuring their intensity difference. The time dependence of the magnetization is given by:

$$\frac{d}{dt} \begin{bmatrix} E/2 \\ I_x^A \\ I_y^A \\ I_z^A \\ I_x^B \\ I_y^B \\ I_z^B \\ I_x^C \\ I_y^C \\ I_z^C \end{bmatrix} = - \begin{bmatrix} 0 & 0 & 0 & 0 & 0 & 0 & 0 & 0 & 0 \\ 0 & \lambda^A + k_1 + k_2 & \Omega^A & -\omega_y & -k_{-1} & 0 & 0 & 0 & -k_{-2} \\ 0 & -\Omega^A & \lambda^A + k_1 + k_2 & \omega_x & 0 & -k_{-1} & 0 & 0 & 0 \\ -2\Theta^A & \omega_y & -\omega_x & \rho^A + k_1 + k_2 & 0 & 0 & -k_{-1} & 0 & 0 \\ 0 & -k_1 & 0 & 0 & \lambda^B + k_{-1} + k_3 & \Omega^B & -\omega_y & -k_{-3} & 0 \\ 0 & 0 & -k_1 & 0 & -\Omega^B & \lambda^B + k_{-1} + k_3 & \omega_x & 0 & 0 \\ -2\Theta^B & 0 & 0 & -k_1 & \omega_y & -\omega_x & \rho^B + k_{-1} + k_3 & 0 & 0 \\ 0 & -k_2 & 0 & 0 & -k_3 & 0 & 0 & \lambda^C + k_{-2} + k_{-3} & \lambda^A + \\ 0 & 0 & -k_2 & 0 & 0 & -k_3 & 0 & -\Omega^C & \omega_y \\ -2\Theta^C & 0 & 0 & -k_2 & 0 & 0 & -k_3 & \omega_y & \lambda^A + \end{bmatrix} \begin{bmatrix} E/2 \\ I_x^A \\ I_y^A \\ I_z^A \\ I_x^B \\ I_y^B \\ I_z^B \\ I_x^C \\ I_y^C \\ I_z^C \end{bmatrix} \quad (1)$$

where  $I$  represents the magnetizations of the  $^{15}\text{N}$  spins in the rotating frame in the free monomer, and in the tethered and direct-contact protofibril-bound states (denoted by the superscripts  $A$ ,  $B$  and  $C$ , respectively). The relaxation rates for transverse and longitudinal magnetization are  $\lambda$  and  $\rho$ , respectively;  $\Omega$  is the resonance offset frequency calculated as the difference between the peak resonance frequency (accounting for peak folding in the case of A $\beta$ 42 Ala42) and the  $^{15}\text{N}$  carrier frequency + CW pulse offset, and  $\omega$  the RF field strength of the CW saturation pulse applied along the appropriate axis;  $E$  is unity; and  $\Theta$  is related to the equilibrium magnetization as described by Helgstrand et al<sup>23</sup>. The rate constants are as follows (see Fig. 2b):  $k_1$  and  $k_2$  are the apparent first order rate constants for the forward reaction from the monomer to the tethered and direct-contact protofibril-bound states, respectively;  $k_{-1}$  and  $k_{-2}$  are the corresponding dissociation rate constants and in this instance  $k_{-1} = k_{-2}$  (see main text);  $k_3$  and  $k_{-3}$  (not shown in Fig. 2b) are the rate constants for the conversion of tethered to direct-contact states, and vice versa, respectively. Detailed balance is ensured from the relationship  $k_{-3} = k_3 k_1 / k_2$  (with  $k_{-1} = k_{-2}$ ). The numerical solution for  $I_z^A$ , the experimentally observed magnetization in the DEST experiment, after a given saturation time as a function of frequency offset was calculated using the matrix exponential function in the program Matlab. The solution is calculated for both initial  $^{15}\text{N}$  magnetization during the saturation period on the  $+z$  and  $-z$  axes,  $I_{+z}$  and  $I_{-z}$ , and the difference,  $I_{+z} - I_{-z}$ , is then computed at each frequency offset and RF field strength, normalized to the solution without saturation, and compared to the normalized experimentally observed intensity.

$R_2$  values, for a given set of kinetic and relaxation rate constants, were calculated by subtracting the monomer  $^{15}\text{N}$ - $R_2$  values for each residue, measured experimentally on the monomeric 50  $\mu\text{M}$  samples, from the calculated  $R_2$  values. The calculated  $R_2$  value for a system in equilibrium exchange is computed assuming a single exponential decay:

$$R_2^{calc} = -\ln\left(\frac{I_x^A(\tau)}{I_x^A(0)}\right) / \tau \quad (2)$$

where the transverse magnetization,  $I_x^A$ , is computed at time  $\tau = 0.2$  s and time 0. The choice of 0.2 s for  $\tau$  was chosen to match to one of the longer delays used in the experimental  $^{15}\text{N}$ - $R_2$  measurements. Simulated delays longer than  $\approx 20$  ms result in the same value of  $R_2^{calc}$ , validating the assumption of single exponential decay.

$^{15}\text{N}$  relaxation rates in the protofibril-bound states, and kinetic rate constants connecting monomer and protofibril-bound states in all schemes (cf. Fig. 2) were fit by simultaneous non-linear least squares minimization of the differences between the observed and calculated (Eq. 1) DEST profiles (at both applied RF field strengths for the CW  $^{15}\text{N}$  saturation pulse) and between the observed and calculated (Eq. 2)  $R_2$  values.

## Supplementary Material

Refer to Web version on PubMed Central for supplementary material.

## Acknowledgements

We thank Rob Tycko for useful discussions, Dusty Baber, Dan Garrett and Mengli Cai for NMR technical assistance, Frank Shewmaker for performing dot blots, and Wei Qiang, Bo Chen and Kent Thurber for assistance with AFM and EM imaging. This work was supported by the intramural program of NIDDK/NIH and the AIDS Targeted Antiviral Program of the NIH Director (to G.M.C.).

## References

1. Lashuel HA, Lansbury PT. Are amyloid diseases caused by protein aggregates that mimic bacterial pore-forming toxins? *Q. Rev. Biophys.* 2006; 39:167–201. [PubMed: 16978447]
2. Walsh DM, Selkoe DJ. A beta Oligomers - a decade of discovery. *J. Neurochem.* 2007; 101:1172–1184. [PubMed: 17286590]
3. Glabe CG. Structural classification of toxic amyloid oligomers. *J. Biol. Chem.* 2008; 283:29639–29643. [PubMed: 18723507]
4. Querfurth HW, LaFerla FM. Mechanisms of Disease Alzheimer's Disease. *New Eng. J. Med.* 2010; 362:329–344. [PubMed: 20107219]
5. Ahmed M, et al. Structural conversion of neurotoxic amyloid- $\beta$  (1–42) oligomers to fibrils. *Nature Struct Mol. Biol.* 2010; 17 561-U556.
6. Fukumoto H, et al. High-molecular-weight beta-amyloid oligomers are elevated in cerebrospinal fluid of Alzheimer patients. *FASEB J.* 2010; 24:2716–2726. [PubMed: 20339023]
7. Petkova AT, et al. A structural model for Alzheimer's beta-amyloid fibrils based on experimental constraints from solid state NMR. *Proc. Natl. Acad. Sci. U. S. A.* 2002; 99:16742–16747. [PubMed: 12481027]
8. Luhrs T, et al. 3D structure of Alzheimer's amyloid-beta(1–42) fibrils. *Proc. Natl. Acad. Sci. U. S. A.* 2005; 102:17342–17347. [PubMed: 16293696]
9. Paravastu AK, Leapman RD, Yau WM, Tycko R. Molecular structural basis for polymorphism in Alzheimer's beta-amyloid fibrils. *Proc. Natl. Acad. Sci. U. S. A.* 2008; 105:18349–18354. [PubMed: 19015532]
10. Petkova AT, Yau WM, Tycko R. Experimental constraints on quaternary structure in Alzheimer's  $\beta$ -amyloid fibrils. *Biochemistry.* 2006; 45:498–512. [PubMed: 16401079]
11. Fawzi NL, Okabe Y, Yap EH, Head-Gordon T. Determining the critical nucleus and mechanism of fibril elongation of the Alzheimer's A $\beta$ (1–40) peptide. *J. Mol. Biol.* 2007; 365:535–550. [PubMed: 17070840]
12. Powers ET, Powers DL. Mechanisms of protein fibril formation: nucleated polymerization with competing off-pathway aggregation. *Biophys. J.* 2008; 94:379–391. [PubMed: 17890392]
13. Jarrett JT, Berger EP, Lansbury PT Jr. The carboxy terminus of the beta amyloid protein is critical for the seeding of amyloid formation: implications for the pathogenesis of Alzheimer's disease. *Biochemistry.* 1993; 32:4693–4697. [PubMed: 8490014]
14. Riek R, Guntert P, Dobeli H, Wipf B, Wuthrich K. NMR studies in aqueous solution fail to identify significant conformational differences between the monomeric forms of two Alzheimer peptides with widely different plaque-competence, A $\beta$ (1–40)(ox) and A $\beta$ (1–42)(ox). *Eur. J. Biochem.* 2001; 268:5930–5936. [PubMed: 11722581]
15. Fawzi NL, Ying J, Torchia DA, Clore GM. Kinetics of amyloid  $\beta$  monomer-to-oligomer exchange by NMR relaxation. *J. Am. Chem. Soc.* 2010; 132:9948–9951. [PubMed: 20604554]
16. Teplow DB, et al. Elucidating amyloid beta-protein folding and assembly: a multidisciplinary approach. *Acc. Chem. Res.* 2006; 39:635–645. [PubMed: 16981680]
17. Mastrangelo IA, et al. High-resolution atomic force microscopy of soluble A $\beta$ 42 oligomers. *J. Mol. Biol.* 2006; 358:106–119. [PubMed: 16499926]
18. Pimplikar SW. Reassessing the amyloid cascade hypothesis of Alzheimer's disease. *Int. J. Biochem. Cell Biol. J.* 2009; 41:1261–1268.
19. Scheidt HA, Morgado I, Rothemund S, Huster D, Fandrich M. Solid-state NMR spectroscopic investigation of A $\beta$  protofibrils: implication of a  $\beta$ -sheet remodeling upon maturation into terminal amyloid fibrils. *Angewandte Chemie.* 2011; 50:2837–2840. [PubMed: 21387500]

20. Hou LM, et al. Solution NMR studies of the A $\beta$ (1–40) and A $\beta$ (1–42) peptides establish that the met35 oxidation state affects the mechanism of amyloid formation. *J. Am. Chem. Soc.* 2004; 126:1992–2005. [PubMed: 14971932]
21. Yan Y, Wang C. A $\beta$ 42 is more rigid than A $\beta$ 40 at the C terminus: implications for Abeta aggregation and toxicity. *J. Mol. Biol.* 2006; 364:853–862. [PubMed: 17046788]
22. McConnell HM. Reaction rates by nuclear magnetic resonance. *J. Chem. Phys.* 1958; 28:430–431.
23. Helgstrand M, Hard T, Allard P. Simulations of NMR pulse sequences during equilibrium and non-equilibrium chemical exchange. *J. Biomol. NMR.* 2000; 18:49–63. [PubMed: 11061228]
24. Lee J, Culyba EK, Powers ET, Kelly JW. Amyloid- $\beta$  forms fibrils by nucleated conformational conversion of oligomers. *Nature Chem. Biol.* 2011; 7:602–609. [PubMed: 21804535]
25. Carulla N, et al. Molecular recycling within amyloid fibrils. *Nature.* 2005; 436:554–558. [PubMed: 16049488]
26. Carulla N, Zhou M, Giralt E, Robinson CV, Dobson CM. Structure and intermolecular dynamics of aggregates populated during amyloid fibril formation studied by hydrogen/deuterium exchange. *Acc. Chem. Res.* 2010; 43:1072–1079. [PubMed: 20557067]
27. Hansen DF, Vallurupalli P, Kay LE. Measurement of methyl group motional parameters of invisible, excited protein states by NMR spectroscopy. *J. Am. Chem. Soc.* 2009; 131:12745–12754. [PubMed: 19685870]
28. Ishima R, Torchia DA. Accuracy of optimized chemical-exchange parameters derived by fitting CPMG R2 dispersion profiles when  $R_2(0a)$  not =  $R_2(0b)$ . *J. Biomol. NMR.* 2006; 34:209–219. [PubMed: 16645811]
29. Ruschak AM, Religa TL, Breuer S, Witt S, Kay LE. The proteasome antechamber maintains substrates in an unfolded state. *Nature.* 2010; 467:868–871. [PubMed: 20944750]
30. Sugase K, Dyson HJ, Wright PE. Mechanism of coupled folding and binding of an intrinsically disordered protein. *Nature.* 2007; 447:1021–1025. [PubMed: 17522630]
31. Sklenar V, Torchia D, Bax A. Measurement of  $^{13}\text{C}$  longitudinal relaxation using  $^1\text{H}$  detection. *J. Magn. Reson.* 1987; 73:375–379.
32. Delaglio F, et al. NmrPipe - a multidimensional spectral processing system based on Unix pipes. *J. Biomol. NMR.* 1995; 6:277–293. [PubMed: 8520220]

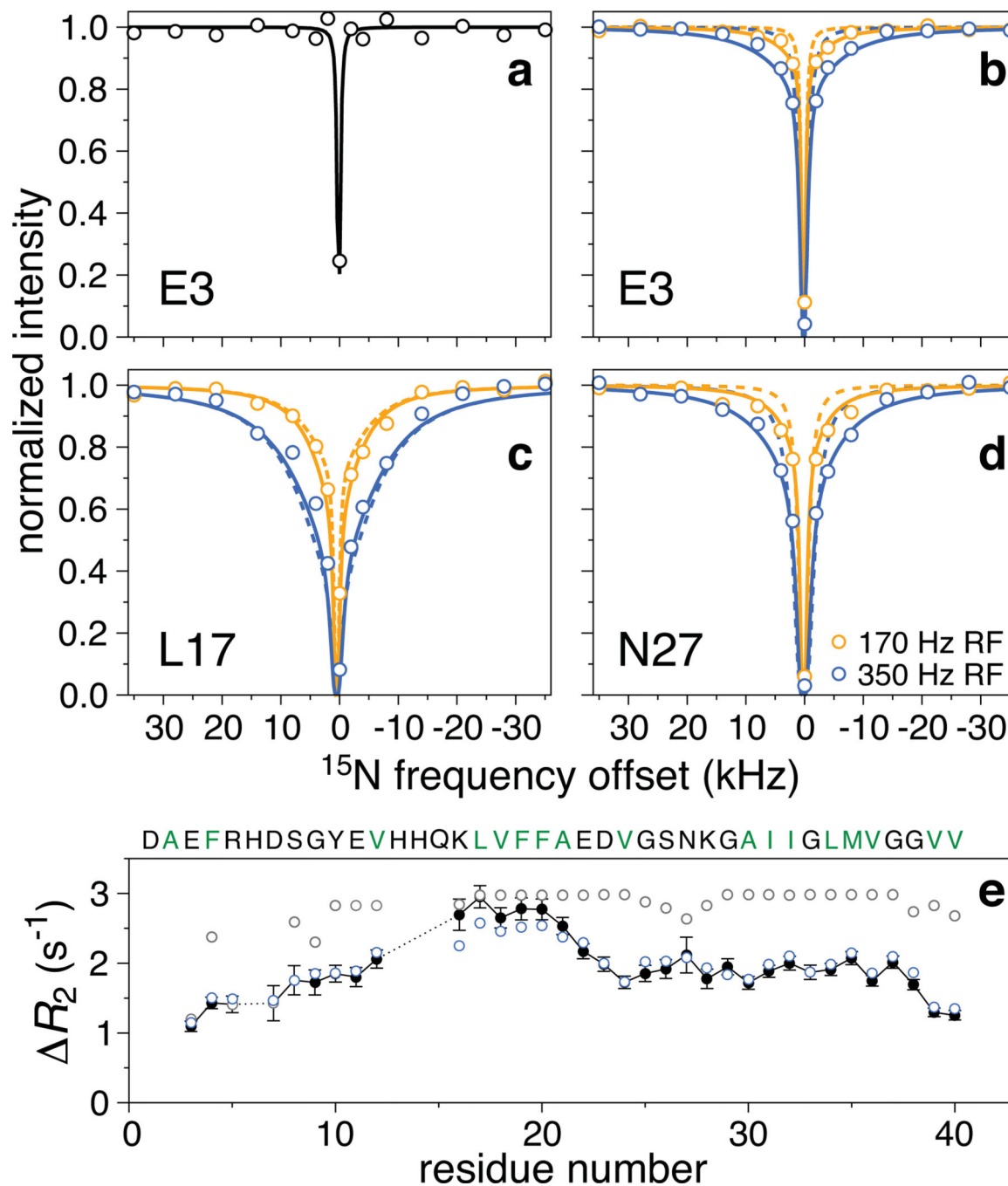


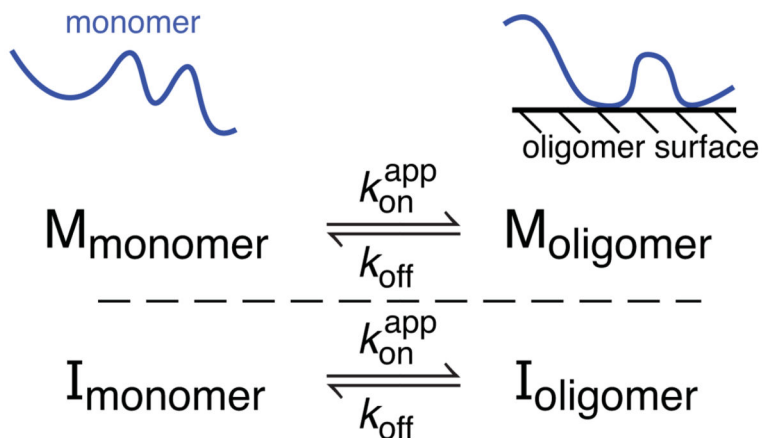
**Figure 1.  $^{15}\text{N}$  Dark-state exchange saturation transfer (DEST) and  $R_2$  for  $\text{A}\beta_{40}$**

Examples of normalized cross-peak intensities as a function of frequency offset from the  $^{15}\text{N}$  carrier (118.5 ppm): **a**, Glu-3 in the 50  $\mu\text{M}$   $\text{A}\beta_{40}$  sample (RF field strength of  $^{15}\text{N}$  saturation pulse = 170 Hz); **b**, **c** and **d**, Glu-3, Leu-17 and Asn-27, respectively, in the 270  $\mu\text{M}$   $\text{A}\beta_{40}$  sample with  $^{15}\text{N}$  saturation at RF field strengths of 170 (orange circles) and 350 (blue circles) Hz. The solid line in (a) is the calculated saturation profile for a  $^{15}\text{N}$  spin with the experimentally determined relaxation rates for monomeric  $\text{A}\beta_{40}$ . The dashed and solid lines in (b)–(d) are the best-fits to an exchange model with a single protofibril-bound state

(cf. Fig. 2a) and to a model incorporating residues tethered and in direct contact with the protofibril (cf. Fig. 2b), respectively. The s.d. of the DEST experimental data points is approximately equal to the size of the circles. **e**, Observed (black filled-in circles; error bars: 1 s.d.) versus calculated  $R_2$  values for the first (grey circles) and second (blue circles) models. The reduced  $\chi^2$  for the simultaneous best-fit to the DEST and  $R_2$  data is 9.0 for the first model and 1.8 for the second.

**a**

overall exchange process  
same for each residue



**b**

oligomer-state exchange  
on a residue-specific basis

$$k_{on}^{app} = k_1^{app(i)} + k_2^{app(i)}$$

$$k_{off} = k_{-1}$$

$$\frac{[I_{directly-bound}(i)]}{[I_{tethered}(i)]} = k_2^{app(i)} / k_1^{app(i)} = K_3(i)$$

$$[M_{monomer}] = [I_{monomer}(i)]$$

$$[M_{oligomer}] = [I_{tethered}(i)] + [I_{directly-bound}(i)]$$

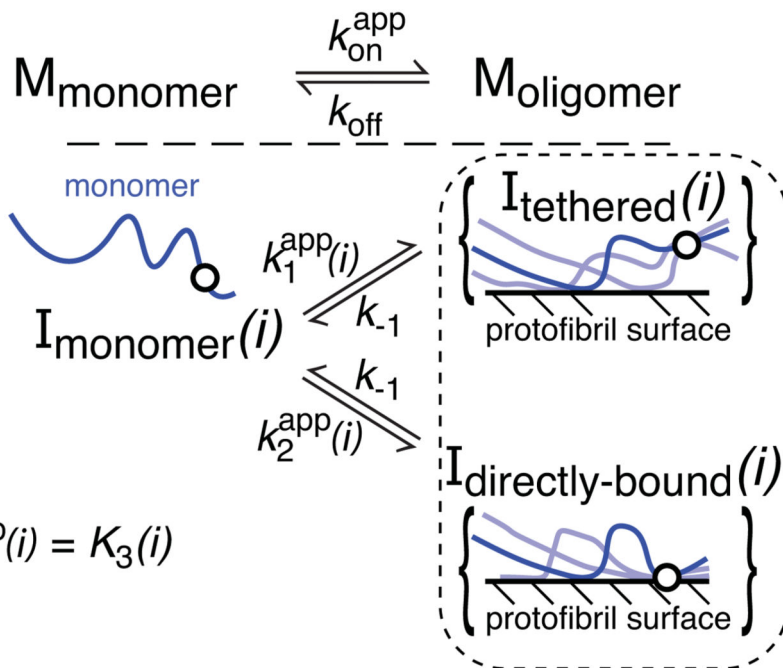


**Figure 2. Kinetic schemes for monomer exchange on the surface of A $\beta$  protofibrils**

**a**, The protofibril-bound peptide ( $M_{oligomer}$ ) exists in only a single state. **b**, The protofibril-bound peptide exists as a large ensemble of states such that each residue can be either tethered or in direct contact with the surface of the oligomer with  $K_3(i) = k_2^{app(i)} / k_1^{app(i)}$ . The circle in the diagrammatic representation of the states represents a single residue that is either tethered or in direct contact and for which three possible chain configurations are shown.



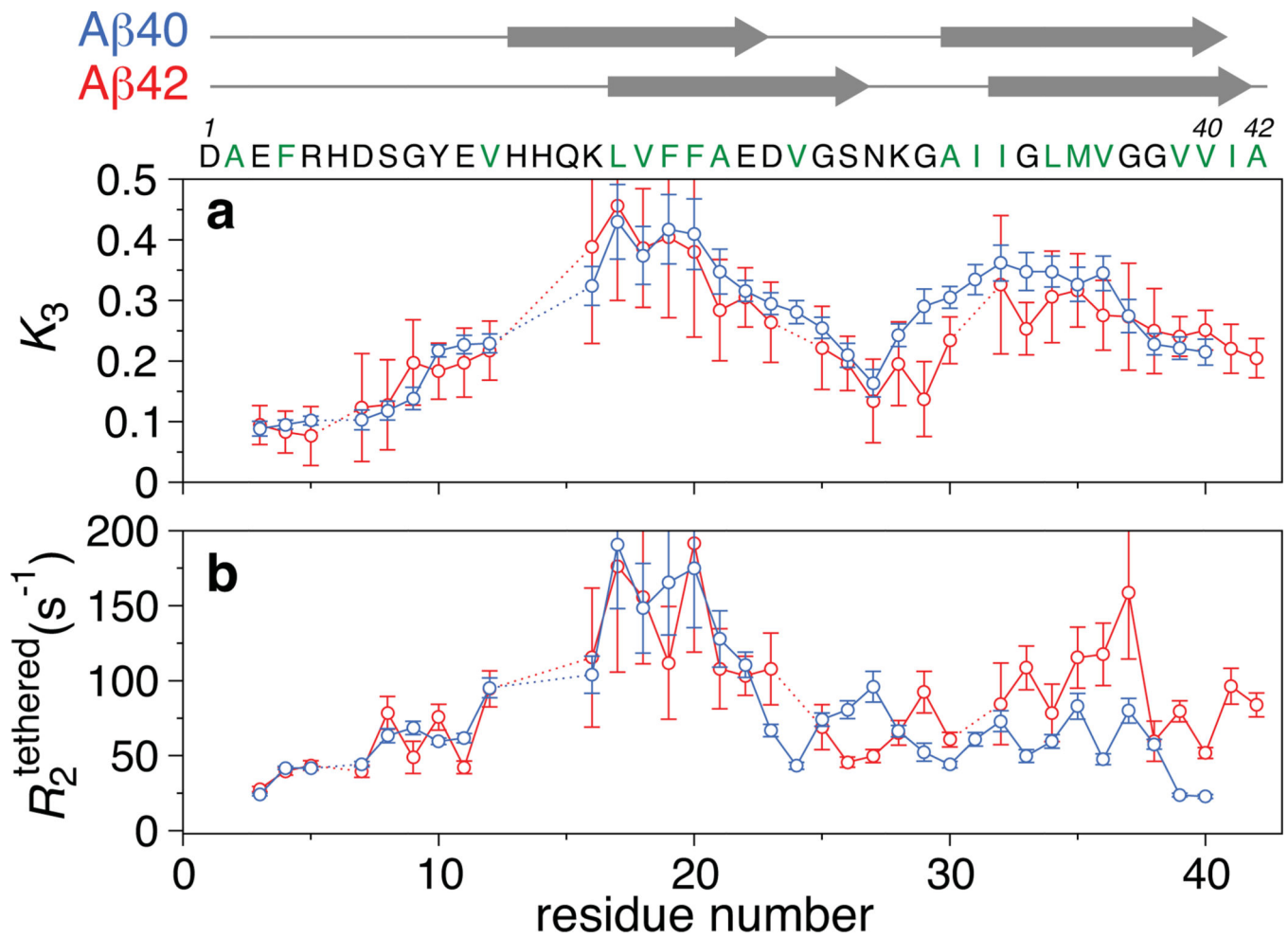


**Figure 3. Comparison of residue-specific fitted parameters describing the ensemble of protofibril-bound states**

**a.** Residue-specific equilibrium constant ( $K_3$ ) for the relative partitioning of direct-contact and tethered states of the oligomer. **b.**  $^{15}\text{N} - R_2^{\text{tethered}}$  values for the tethered states. The values for Aβ40 and Aβ42 are displayed as blue and red circles, respectively. The proposed two β-strand regions in fibrils of Aβ40<sup>9</sup> and Aβ42<sup>8</sup> are indicated by arrows at the top of the figure. Error bars: 1 s.d.